

Giant anisotropic nonlinear optical response in transition metal monpnictide Weyl semimetals

Liang Wu,^{1,2,*} Shreyas Patankar,^{1,2} Takahiro Morimoto,¹ Nityan L. Nair,¹ Eric Thewalt,^{1,2} Arielle Little,^{1,2} James G. Analytis,^{1,2} Joel E. Moore,^{1,2} and J. Orenstein^{1,2,†}

¹*Department of Physics, University of California, Berkeley, California 94720, USA*

²*Materials Science Division, Lawrence Berkeley National Laboratory, Berkeley, California 94720, USA*

(Dated: September 1, 2022)

Although Weyl fermions have proven elusive in high-energy physics, their existence as emergent quasiparticles was recently predicted in certain crystalline solids in which either inversion or time-reversal symmetry is broken[1–4]. The subsequent search for Weyl fermions in condensed matter soon led to their detection[5–7] in transition metal monpnictides (TMMPs) such as TaAs, a class of noncentrosymmetric materials that heretofore received only limited attention. Now that the Weyl semimetal state in TMMPs is confirmed, the question arises as to whether these materials will exhibit novel, enhanced, or technologically applicable electronic properties. The TMMPs are polar metals, a rare subset of inversion-breaking crystals that would allow spontaneous polarization, were it not screened by conduction electrons[8–10]. Despite the absence of spontaneous polarization, polar metals can exhibit other signatures of inversion-symmetry breaking, most notably second-order nonlinear optical polarizability, $\chi^{(2)}$, leading to phenomena such as optical rectification and second-harmonic generation (SHG). Here we report measurements of SHG that reveal a giant, anisotropic $\chi^{(2)}$ in the TMMPs TaAs, TaP, and NbAs. With the fundamental and second harmonic fields oriented parallel to the polar axis, the value of $\chi^{(2)}$ is larger by almost one order of magnitude than its value in the archetypal electro-optic materials GaAs and ZnTe, and in fact larger than reported in any crystal to date.

The last decade has witnessed an explosion of research investigating the role of bandstructure topology, as characterized for example by the Berry curvature in momentum space, in the electronic response functions of crystalline solids[11]. While the best established example is the intrinsic anomalous Hall effect in time-reversal breaking systems[12], several nonlocal[13, 14] and nonlinear effects related to Berry curvature generally[15, 16] and in WSM's specifically[17, 18] have been predicted in crystals that break inversion symmetry. Of these, the most relevant to this work is a theoretical formulation[19] of

SHG in terms of the shift vector, which is a quantity related to the difference in Berry connection between two bands that participate in an optical transition.

Fig. 1(a) and caption provide a schematic and description of the optical set-up for measurement of SHG in TMMP crystals. Figs. 1(b) and 1(c) show results from a (112) surface of TaAs. The SH intensity from this surface was very strong, allowing for polarization rotation scans with signal-to-noise ratio above 10^6 . In contrast, SHG from a TaAs (001) surface was barely detectable (at least six orders of magnitude lower than (112) surface). Below, we describe the use of the set-up shown in Fig. 1(a) to characterize the second-order optical susceptibility tensor, χ_{ijk} , defined by the relation, $P_i(2\omega) = \epsilon_0 \chi_{ijk} E_j(\omega) E_k(\omega)$.

As a first step, we determined the orientation of the high-symmetry axes in the (112) surface, which are the [1,-1,0] and [1,1,-1] directions. To do so, we simultaneously rotated the linear polarization of the generating light (the generator) and the polarizer placed before the detector (the analyzer), with their relative angle set at either 0° or 90° . Rotating the generator and analyzer together produces scans, shown in Figs. 1(b) and 1(c), that are equivalent to rotation of the sample about the surface normal. The angle at which we observe the peak and the null in Fig. 1(b) and the null in Fig. 1(c) allow us to identify the principle axes in the (112) plane of the surface.

Having determined the high symmetry directions, we characterize χ_{ijk} by performing three of types of scans, the results of which are shown in Fig. 2. In scans shown in Figs. 2(a) and (b), we oriented the analyzer along one of the two high symmetry directions and rotated the plane of linear polarization of the generator through 360° . Fig. 2(c) shows the circular dichroism of the SHG response, that is, the difference in SH generated by left and right circularly polarized light. For all three scans the SHG intensity as a function of angle is consistent with the second-order optical susceptibility tensor expected for the $4mm$ point group of TaAs, as indicated by the high accuracy of the fits in Fig. 1(b),(c) and Fig. 2(a)-(c).

In the $4mm$ structure xz and yz are mirror planes but reflection through the xy plane is not a symmetry; therefore TaAs is an acentric crystal with an unique polar (z) axis. In crystals with $4mm$ symmetry there are three independent nonvanishing elements of χ_{ijk} : χ_{zzz} , $\chi_{zxx} = \chi_{zyy}$, and $\chi_{xzx} = \chi_{yzy} = \chi_{xxz} = \chi_{yyz}$. Note

*Electronic address: liangwu@berkeley.edu

†Electronic address: jworenstein@lbl.gov

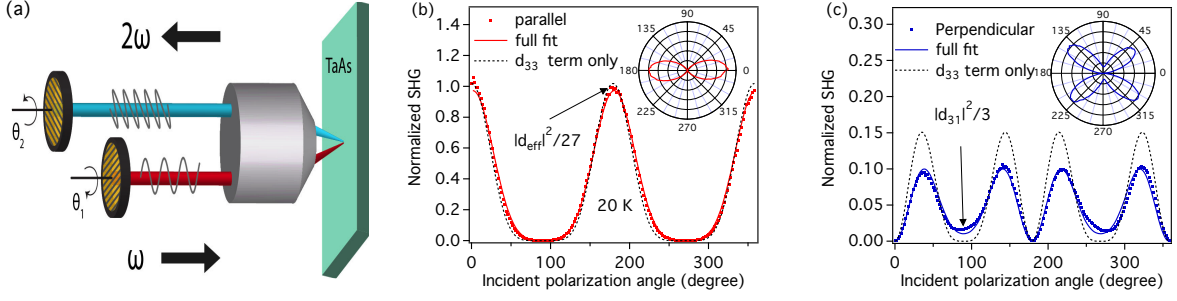


FIG. 1: (Color online) **Second harmonic generation vs. angle as TaAs is effectively rotated about the axis perpendicular to the (112) surface.** (a), Schematic of SHG experimental setup. To stimulate second harmonic light, pulses of 800 nm wavelength (ω frequency) were focused at near normal incidence to a 10 micron diameter spot on the sample. Polarizers and waveplates mounted on rotating stages allowed for continuous and independent control of the polarization of the generating and second-harmonic (2ω frequency) light that reached the detector. θ_1 and θ_2 are the angle of the polarization plane after the generator and the analyzer respectively with respect to the [1,1,-1] crystal axis. (b), (c) SHG intensity as a function of angle of incident polarization at 20 K. In (b) and (c) the analyzer is parallel and perpendicular to the generator, respectively. In both plots the amplitude is normalized by the peak value in (b). The solid lines are fits that include all the allowed tensor elements in $4mm$ symmetry, whereas the dashed lines include only d_{33} . The insets are polar plots of measured SHG intensity vs. incident polarization angle.

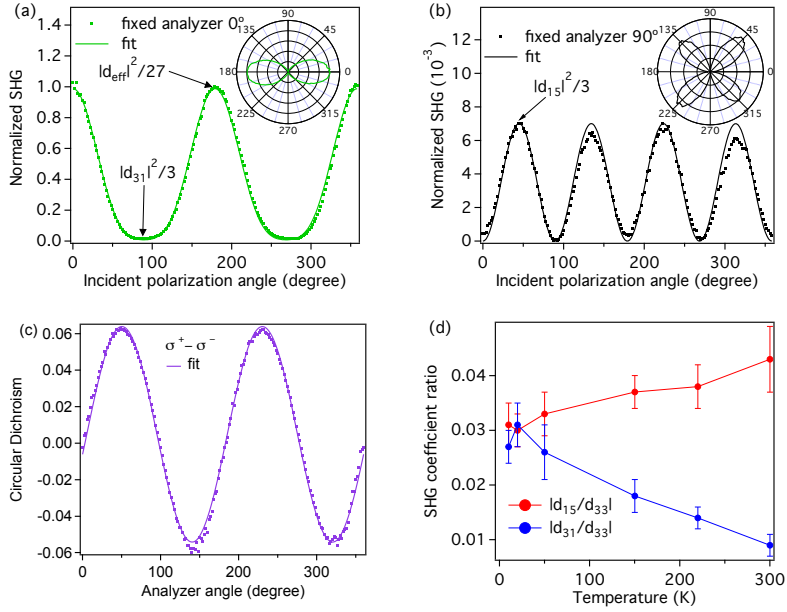


FIG. 2: (Color online) **Second harmonic intensity as function of generator polarization with fixed analyzer.** Analyzers are fixed along (a) 0° and (b) 90° , which are [1,1,-1] and [1,-1,0] crystal axes, respectively. Solid lines are fits considering all three non-zero tensor elements with expressions: $I_{0^\circ} = |d_{\text{eff}} \cos^2 \theta_1 - d_{31} \sin^2 \theta_1|/27$ and $I_{90^\circ} = (|d_{15}|^2 \sin 2\theta_1)/3$. The insets are polar plots of measured SHG intensity. (c) Normalized circular dichroism (SHG intensity difference between right- and left-hand circularly polarized generation light) vs. polarization angle of the analyzer at 300 K. The solid line is a fit. (d) Temperature dependence of $|d_{15}/d_{33}|$ and $|d_{31}/d_{33}|$. The estimation of error bars can be found in methods.

that each has at least one z component, implying null electric dipole SHG when all fields are in the xy plane. This is consistent with observation of nearly zero SHG for light incident on the (001) plane. Below, we follow the convention of using the 3×6 second-rank tensor d_{ij} , rather than χ_{ijk} , to express the SHG response, where the relation between the two tensors for TaAs is: $d_{33} = \chi_{zzz}$,

$d_{31} = \chi_{zzx}$, and $d_{15} = \chi_{xzx}/2$ (Supplementary Information section IV A).

Starting with the symmetry constrained d tensor, we derive expressions, specific to the (112) surface, for the angular scans with fixed analyzer shown in Fig. 2 (Supplementary Information section IV A). We obtain $|d_{\text{eff}} \cos^2 \theta_1 - d_{31} \sin^2 \theta_1|^2/27$ and $|d_{15}|^2 \sin 2\theta_1/3$ for an-

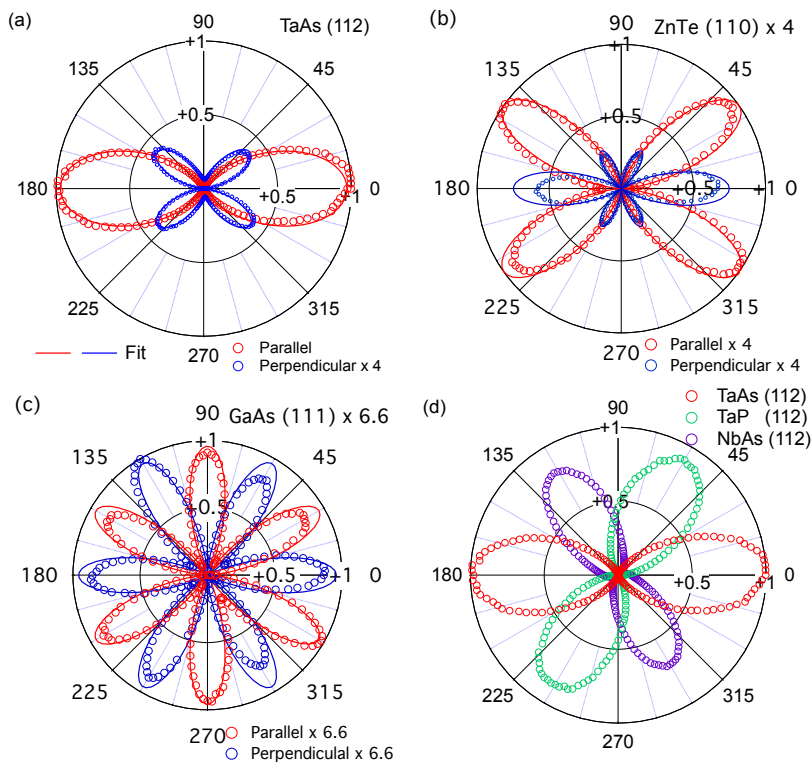


FIG. 3: (Color online) **Benchmark SHG experiments on TaAs (112), TaP (112), NbAs (112), ZnTe (110) and GaAs (111).** SHG polar plots in the same scale for TaAs (112) (a), ZnTe (110) (b), and GaAs (111) (c) in both the parallel and perpendicular generator/analyzer configurations at room temperature. For TaAs data the perpendicular configuration is magnified by a factor of 4 for clarity. The SHG intensity of ZnTe and GaAs are multiplied by a factor 4 and 6.6 respectively to match the peak value of TaAs. (d), SHG polar plots for TaAs (112), TaP (112) and NbAs (112) in the parallel configurations at room temperature with plots of TaP and NbAs rotated by 60° and 120° for clarity.

alyzer parallel to $[1,1,-1]$ and $[1,-1,0]$, respectively, where $d_{\text{eff}} \equiv d_{33} + 2d_{31} + 4d_{15}$. Fits to these expressions yield two ratios: $|d_{\text{eff}}/d_{15}|$ and $|d_{\text{eff}}/d_{31}|$. Although we do not determine $|d_{33}/d_{15}|$ and $|d_{33}/d_{31}|$ directly, it is clear from the extreme anisotropy of the angular scans that d_{33} , which gives the SHG response when both generator and analyzer are parallel to the polar axis, is much larger than the other two components. We can place bounds on $|d_{33}/d_{15}|$ and $|d_{33}/d_{31}|$ by setting d_{15} and d_{31} in and out of phase with d_{33} . We note that the observation of circular dichroism in SHG, shown in Fig. 2(c), indicates that relative phase between d_{15} and d_{33} is neither 0° or 180° , but rather closer to 30° (Supplementary Information section IV A).

The results of this analysis are plotted in Fig. 2(d), where it is shown that $|d_{33}/d_{15}|$ falls in the range $\sim 25 - 33$ for all temperature, and $|d_{33}/d_{31}|$ increases from ~ 30 to ~ 100 with increasing temperature. Perhaps because of its polar metal nature, the anisotropy of the second-order susceptibility in TaAs is exceptionally large compared with what has been observed previously in crystals with the same set of nonzero d_{ij} . For example, α -ZnS, CdS, and KNiO_3 have $|d_{31}| \cong |d_{15}| \cong d_{33}/2$ [20], while in BaTiO_3 the relative sizes are reversed, with

$$|d_{31}| \cong |d_{15}| \approx 2|d_{33}|[21].$$

Even more striking than the extreme anisotropy of χ_{ijk} is the absolute size of the SHG response in TaAs. The search for materials with large second-harmonic optical susceptibility has been of continual interest since the early years of nonlinear optics[22]. To determine the absolute magnitude of the d coefficients in TaAs we used GaAs and ZnTe as benchmark materials. Both crystals have large and well characterized second-order optical response functions[7, 8], with GaAs regarded as having among the largest $\chi_{ijk}^{(2)}$ of any known material. GaAs and ZnTe are also ideal as benchmarks because their response tensors have only one nonvanishing coefficient, $d_{14} \equiv 2\chi_{xyz}$.

Figs. 3(a)-(c) show polar plots of SHG intensity as TaAs (112), ZnTe (110), and GaAs (111) are (effectively) rotated about the optic axis with the generator and analyzer set at 0° and 90° . Also shown (as solid lines) are fits to the polar patterns obtained by rotating the $\chi^{(2)}$ tensor to a set of axes that includes the surface normal, which is (110) and (111) for our ZnTe and GaAs crystals respectively (Supplementary Information Section V.A). Even prior to analysis to extract the ratio of d coefficients between the various crystals, it is clear that the SHG re-

sponse of TaAs(112) is large, as the peak intensity in this geometry exceeds ZnTe (110) by a factor of 4.0 and GaAs (111) by a factor of 6.6. Fig. 3(d) compares the parallel polarization data for TaAs shown in Fig. 3(a) with SHG measured under the same conditions in the TMMP's TaP and NbAs (112) facets. The strength of SHG from the three crystals, which share the same $4mm$ point group, is clearly very similar, with TaP and NbAs intensities relative to TaAs of $0.90(\pm 0.02)$ and $0.76(\pm 0.04)$, respectively. The SHG response in these compounds is also dominated by the d_{33} coefficient. Finally, we found that the SHG intensity of all three compounds does not decrease after exposure to atmosphere for several months.

To obtain the response of TMMP's relative to the two benchmark materials we used the Bloembergen-Pershan formula [22] to correct for the variation in specular reflection of SH light that results from the small differences in the index of refraction of the three materials at the fundamental and SH frequency. (Details concerning this correction, which is less than 20%, can be found in supplementary Information section IV B). Table I presents the results of this analysis, showing that $|d_{33}| \cong 3600$ pm/V at fundamental wavelength 800 nm in TaAs exceeds values in benchmark materials GaAs [8] and ZnTe [7] by approximately one order of magnitude, even when measured at wavelengths where their response is largest. The d coefficient in TaAs at 800 nm exceeds corresponding values in ferroelectric materials BiFeO₃ [25], BaTiO₃ [21], LiNbO₃ [20] by two orders of magnitude. In the case of the ferroelectric materials, SHG measurements have not been performed in their spectral regions of strong absorption, typically 3-7 eV. However, *ab-initio* calculations consistently predict that the resonance enhanced d values in this region do not exceed roughly 500 pm/V [26, 27].

| Material | $ d_{ij} $ | $ d $ (pm/V) | Fundamental wavelength (nm) | Reference |
|--------------------|------------|--------------------|-----------------------------|--------------------------|
| TaAs | d_{33} | 3600 (± 550) | 800 | This work |
| GaAs | d_{14} | 350* | 810 | Ref. 8 |
| ZnTe | d_{14} | 250, 450* | 800, 700 | Ref. 7 |
| BaTiO ₃ | d_{33} | 15 | 900 | Ref. 21 |
| BiFeO ₃ | d_{33} | 15-19 | 1550, 800 | Ref. 25, 26 ^t |
| LiNbO ₃ | d_{33} | 26 | 852 | Ref. 20 |
| BiFeO ₃ | d_{33} | 250* | 500 | Ref. 26 ^t |
| BaTiO ₃ | d_{33} | 200* | 170 | Ref. 27 ^t |
| PbTiO ₃ | d_{33} | 400* | 150 | Ref. 27 ^t |

TABLE I: Second harmonics generation coefficients of different materials. * denotes the peak value of the material. ^t denotes theoretical calculation. The estimation of error bars can be found in methods.

The results described above raise the question of why χ_{zzz} in the TMMP's is so large. Answering this question quantitatively will require further work in which measurements of $\chi^{(2)}$ as a function of frequency are compared with theory based on *ab initio* bandstructure and wavefunctions. For the present, we describe a calculation of

$\chi^{(2)}$ using a minimal model of a WSM that is based on the approach to nonlinear optics proposed by Morimoto and Nagaosa (MN)[19]. This theory clarifies the connection between bandstructure topology and SHG, and provides a concise expression with clear geometrical meaning for $\chi^{(2)}$. Hopefully this calculation will motivate the *ab initio* theory that is needed to quantitatively account for the large SH response of the TMMPs and its possible relation to the existence of Weyl nodes.

The MN result for the dominant (zzz) response function is,

$$\text{Re}\{\sigma_{zzz}^{(2)}(\omega, 2\omega)\} \cong \frac{\pi e^3}{2\hbar\omega^2} \int \frac{d^3\mathbf{k}}{(2\pi)^3} |v_{z,12}|^2 R_{zz}(\mathbf{k}) \times \left[-\delta(\epsilon_{21} - \hbar\omega) + \frac{1}{2}\delta(\epsilon_{21} - 2\hbar\omega) \right]. \quad (1)$$

In Eq. 1 the nonlinear response is expressed as a second-order conductivity, $\sigma_{zzz}(\omega, 2\omega)$, relating the current induced at 2ω to the square of the applied electric field at ω , *i.e.*, $J_z(2\omega) = \sigma_{zzz}E_z^2(\omega)$. (The SH susceptibility is related to the conductivity through the relation $\chi^{(2)} = \sigma^{(2)}/2i\omega\epsilon_0$). The indices 1 and 2 refer to the valence and conduction bands, respectively, ϵ_{21} is the transition energy, and $v_{i,12}$ is the matrix element of the velocity operator $v_i = (1/\hbar)\partial H/\partial k_i$. Bandstructure topology appears in the form of the ‘‘shift vector,’’ $R_{zz} \equiv \partial_{k_z}\varphi_{z,12} + a_{z,1} - a_{z,2}$, which is a gauge-invariant length formed from the k derivative of the phase of the velocity matrix element, $\varphi_{12} = \text{Im}\{\log v_{12}\}$, and the difference in Berry connection, $a_i = -i\langle u_n | \partial_{k_i} | u_n \rangle$, between bands 1 and 2. Physically, the shift vector is the k -resolved shift of the intracell wave function for the two bands connected by the optical transition.

We consider the following minimal model for a time-reversal symmetric WSM that supports four Weyl nodes,

$$H = t \left\{ [\cos k_x a + m_y(1 - \cos k_y a) + m_z(1 - \cos k_z a)] \sigma_x + [\sin k_y a + \Delta \cos(k_y a) s_x] \sigma_y + \sin(k_z a) s_x \sigma_z \right\}. \quad (2)$$

Here, σ_i and s_i are Pauli matrices acting on orbital and spin degrees of freedom, respectively, t is a measure of the bandwidth, a is the lattice constant, m_y and m_z are parameters that introduce anisotropy, and inversion breaking is introduced by Δ . The Hamiltonian defined in Eq. 2 preserves two-fold rotation symmetry about the z -axis and the mirror symmetries M_x and M_y . These symmetries form a subset of $4mm$ point group which is relevant to optical properties of TMMP's.

Fig. 4 illustrates the energy levels, topological structure, and SHG spectra that emerge from this model. As shown in Fig. 4(a), pairs of Weyl nodes with opposite chirality overlap at two points, $\mathbf{k} = (\pm\pi, 0, 0)$, in the inversion-symmetric case with $\Delta = 0$. With increasing

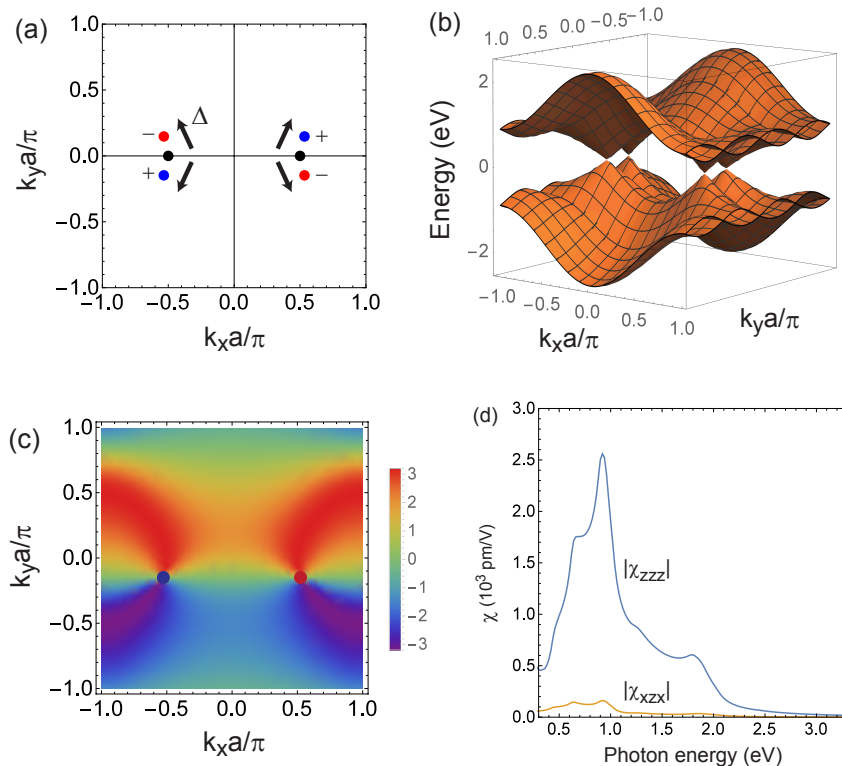


FIG. 4: (Color online) **Numerical results for the second harmonic response of a Weyl semimetal.** (a) Location of Weyl points in the $k_z = 0$ plane for $\Delta = 0.5$. For $\Delta = 0$, Weyl points with opposite chiralities are located at $(\pm\pi/2, 0, 0)$ (denoted by black dots). (b) The band structure for $\Delta = 0.5$ and $k_z = 0$. (c) Color plot of $|v_{12}|^2 R_{zz}$ which appears as an integrand in the formula for $\sigma_{zzz}^{(2)}$. For clarity we plot only $|v_{12}|^2 R_{zz}$ for $s_x = +1$ bands with Weyl points located at $k_y < 0$ (the variation of $|v_{12}|^2 R_{zz}(\mathbf{k})$ for the $s_x = -1$ bands is obtained from the transformation $\mathbf{k} \rightarrow -\mathbf{k}$). $|v_{12}|^2 R_{zz}$ shows structures at Weyl points. (d) $|\chi_{zzz}|$ and $|\chi_{xzx}|$ plotted as a function of incident photon energy for $\Delta = 0.5$. We adopted parameters $t = 0.8$ eV, $m_y = 1$, $m_z = 5$.

Δ the nodes displace in opposite directions along the k_y axis, with $\Delta k_y \cong \Delta/a$. The energy of electronic states in $k_z = 0$ plane, illustrating the linear dispersion near the four Weyl points, is shown in Fig. 4(b). Fig. 4(c) shows the corresponding variation of $|v_{12}|^2 R_{zz}(\mathbf{k})$ for the $s_x = +1$ bands whose Weyl points are located at $k_y < 0$ (the variation of $|v_{12}|^2 R_{zz}(\mathbf{k})$ for the $s_x = -1$ bands is obtained from the transformation $\mathbf{k} \rightarrow -\mathbf{k}$). The magnitude of $\sigma^{(2)}$ derived from this model vanishes as $\Delta \rightarrow 0$ and is also sensitive to the anisotropy parameters m_y and m_z . Fig. 4(d) shows that spectra corresponding to parameters $t = 0.8$ eV, $\Delta = 0.5$, $m_z = 5$, and $m_y = 1$ can reproduce the observed amplitude and large anisotropy of $\chi^{(2)}(\omega, 2\omega)$.

As discussed above, our minimal model of an inversion-breaking WSM is intended mainly to motivate further research into the mechanism for enhanced SHG in the TMMP's. However, the model does suggest universal properties of $\chi^{(2)}$ that arise from transitions near Weyl nodes between bands with nearly linear dispersion. According to bulk bandstructure measurements [7], such transitions are expected at energies below approximately 100 meV in TaAs family, corresponding to far-infrared

and THz regimes. In this regime, where the interband excitation is within the Weyl cones, the momentum-averaged $|v_{12}|^2 R_{zz}(\mathbf{k})$ tends to nonzero value, $\langle v^2 R \rangle$, leading to the prediction that $\sigma^{(2)} \rightarrow g(\omega) \langle v^2 R \rangle / \omega^2$ as $\omega \rightarrow 0$. Because $g(\omega)$, the joint density of states for Weyl fermions is proportional to ω^2 , we predict that $\sigma^{(2)}$ approaches a constant (or alternatively $\chi^{(2)}$ diverges as $1/\omega$) as $\omega \rightarrow 0$, even as the linear optical conductivity vanishes in proportion to ω [28]. The $1/\omega$ scaling of SHG and optical rectification is a unique signature of a WSM in low-energy electrodynamics, as it requires the existence of both inversion breaking and point nodes. In real materials, this divergence will be cutoff by disorder and nonzero Fermi energy. Disorder induced broadening, estimated from transport scattering rates [29] and Pauli blocking from nonzero Fermi energy, estimated from optical conductivity [29] and band calculation [3], each suggest a low energy cutoff in the range 1-10 meV.

We conclude by observing that the search for inversion-breaking WSMs has led, fortuitously, to a new class of polar metals with unusually large second-order optical susceptibility. Although WSM's are not optimal for frequency doubling applications in the visible regime be-

cause of their strong absorption, they are promising materials for THz generation and opto-electronic devices such as far-infrared detectors because of their unique scaling in the $\omega \rightarrow 0$ limit. Looking forward, we hope that our findings will stimulate further investigation of non-linear optical spectra in inversion-breaking WSM's for technological applications and in order to identify the defining response functions of Weyl fermions in crystals.

I. METHODS

Crystal growth and structure characterization

Single crystals of TaAs, TaP and NbAs were grown by vapor transport with iodine as the transport agent. First, polycrystalline was produced by mixing stoichiometric amounts of Ta/Nb and As/P and heating the mixture to 1100 °C in an evacuated quartz ampule for 2 days. 500 mg of the resulting powder was then resealed in a quartz ampoule with 100 mg of iodine and loaded into a horizontal two-zone furnace. The temperature of the hot and cold ends were held at 1000 °C and 850 °C, respectively. After 4 days well-faceted crystals up to several millimeters in size were obtained. Crystal structure was confirmed using single-crystal x-ray micro-Laue diffraction at room temperature at the Advanced Light Source.

Optics setup for second harmonic generation

The optical set up for measuring SHG is illustrated in Fig. 1(a). Generator pulses of 100 fs duration and center wavelength 800 nm pass through a mechanical chopper

that provides amplitude modulation at 1 kHz and are focused at near normal incidence onto the sample. Polarizers and waveplates in the beam path are used to vary the direction of linear polarization and to generate circularly polarization. Both the specularly reflected fundamental and the second harmonic beam are collected by a pickoff mirror and directed to a short-pass, band-pass filter combination that allows only the second harmonic light to reach photomultiplier tube (PMT) photodetector. Another wire-grid polarizer placed before the PMT allows for analysis of the polarization of the second harmonic beam. Temperature dependence measurement was performed by mounting TaAs sample in a cold-finger cryostat on a xyz-micrometer stage. Benchmark measurements on TaAs, TaP, NbAs, ZnTe and GaAs were performed at room temperature in atmosphere with the samples mounted on a xyz-micrometer stage to maximize the signal.

Fitting procedure for SHG We first fit data obtained with fixed analyzer at 90°, which is the [1,-1,0] crystal axis, because there is only one free parameter ($|d_{15}|$) in this configuration. With this value for $|d_{15}|$, we then fit data in the three other types of scans discussed in the text with d_{15} and d_{31} set in and out-of phase with d_{33} . This procedure yields upper and lower bounds on the anisotropy ratios $|d_{15}/d_{33}|$ and $|d_{31}/d_{33}|$ that are shown with error bars in Fig. 2(d). In the case of GaAs and ZnTe all scans are fit accurately by the only symmetry allowed free parameter, which is $|d_{14}|$.

-
- [1] Wan, X., Turner, A. M., Vishwanath, A. & Savrasov, S. Topological semimetal and Fermi-arc surface states in the electronic structure of pyrochlore iridates. *Physical Review B*, **83**, 205101 (2011).
 - [2] Burkov, A. & Balents, L. Weyl semimetal in a topological insulator multilayer. *Physical Review Letters*, **107**, 127205 (2011).
 - [3] Weng, H., Fang, C., Fang, Z., Bernevig, B. A. & Dai, X. Weyl semimetal phase in noncentrosymmetric transitionmetal monophosphides. *Physical Review X*, **5**, 011029 (2015).
 - [4] Huang, S.-M. *et al.* A Weyl Fermion semimetal with surface Fermi arcs in the transition metal mononictide TaAs class *Nature Communications*, **6**, 7373 (2015).
 - [5] Xu, S.-Y. *et al.* Discovery of a Weyl fermion semimetal and topological Fermi arcs. *Science*, **349**, 613 (2015).
 - [6] Lv, B. *et al.* Experimental discovery of Weyl semimetal TaAs. *Physical Review X*, **5**, 031013 (2015).
 - [7] Yang, L. *et al.* Weyl semimetal phase in the noncentrosymmetric compound TaAs. *Nature Physics*, **11**, 728 (2015).
 - [8] Anderson, P. & Blount, E. Symmetry considerations on martensitic transformations: "ferroelectric" metals? *Physical Review Letters*, **14**, 217 (1965).
 - [9] Shi, Y. *et al.* A ferroelectric-like structural transition in a metal. *Nature Materials*, **12**, 1024 (2013).
 - [10] Kim, T. *et al.* Polar metals by geometric design. *Nature*, **533**, 68 (2016).
 - [11] Xiao, D., Chang, M.-C. & Niu, Q. Berry phase effects on electronic properties. *Review of Modern Physics*, **82**, 1959 (2010).
 - [12] Nagaosa, N., Sinova, J., Onoda, S., MacDonald, A. H. & Ong, N. P. Anomalous Hall effect. *Review of Modern Physics*, **82**, 1939 (2010).
 - [13] Orenstein, J. & Moore, J. E. Berry phase mechanism for optical gyrotropy in stripe-ordered cuprates. *Phys. Rev. B*, **87**, 165110 (2013).
 - [14] Zhong, S., Orenstein, J. and Moore, J. E. Optical Gyrotropy from Axion Electrodynamics in Momentum Space. *Phys. Rev. Lett.*, **115**, 117403 (2015).
 - [15] Moore, J. E. & Orenstein, J. Confinement-induced Berry phase and helicity-dependent photocurrents. *Phys. Rev. Lett.*, **105**, 165110 (2010).
 - [16] Sodemann, I. & Fu, L. Quantum nonlinear Hall effect induced by Berry curvature dipole in time-reversal invariant materials. *Physical Review Letters*, **115**, 216806 (2015).
 - [17] Ishizuka, H., Hayata, T., Ueda, M. & Nagaosa, N. Emergent Electromagnetic Induction and Adiabatic Charge Pumping in Weyl Semimetals. *arXiv:1607.06537*, (2016).
 - [18] Chan, C.-K., Lindner, N. H., Refael, G., & Lee, P. A. Photocurrents in Weyl semimetals. *arXiv: 1607.07839*, (2016).
 - [19] Morimoto, T. & Nagaosa, N. Topological nature of nonlinear optical effects in solids. *Science Advances*, **2** (2016).
 - [20] Shoji, I., Kondo, T., Kitamoto, A., Shirane, M. & Ito, R. Absolute scale of second-order nonlinear-optical coeffi-

- cients. *JOSA B*, **14**, 2268, (1997).
- [21] Miller, R. C. Optical harmonic generation in single crystal BaTiO₃. *Physical Review*, **134**, A1313, (1964).
- [22] Bloembergen, N. & Pershan, P. Light waves at the boundary of nonlinear media. *Physical Review*, **128**, 606, (1962).
- [23] Bergfeld, S. & Daum, W. Second-harmonic generation in GaAs: Experiment versus theoretical predictions of $\chi^{(2)xyz}$. *Physical Review Letters*, **90**, 036801, (2003).
- [24] Wagner, H. P., Kuhnelt, M., Langbein, W. & Hvam, W. Dispersion of the second-order nonlinear susceptibility in ZnTe, ZnSe, and ZnS. *Physical Review B*, **58**, 10494, (1998).
- [25] Haislmaier, R. C. *et al.* Large nonlinear optical coefficients in pseudo-tetragonal BiFeO₃ thin films. *Applied Physics Letters*, **103**, 031906, (2013).
- [26] Ju, S., Cai, T.-Y. & Guo, G.-Y. Electronic structure, linear, and nonlinear optical responses in magnetoelectric multiferroic material BiFeO₃. *The Journal of Chemical Physics*, **130**, 214708, (2009).
- [27] Young, S. M. & Rappe, A. M. First principles calculation of the shift current photovoltaic effect in ferroelectrics. *Physical Review Letters*, **109**, 116601, (2012).
- [28] Hosur, P., Parameswaran, S. & Vishwanath, A. Charge transport in Weyl semimetals. *Physical Review Letters*, **108**, 046602, (2012).
- [29] Xu, B. *et al.* I. Optical spectroscopy of the Weyl semimetal TaAs *Phys. Rev. B.*, **93**, 121110, (2016).

II. ADDENDUM

We thank B. M. Fregoso, T. R. Gordillo, J. Neaton and Y. R. Shen for helpful discussions and B. Xu for sharing refractive index data of TaAs. Measurements and modeling were performed at the Lawrence Berkeley National Laboratory in the Quantum Materials program supported by the Director, Office of Science, Office of Basic Energy Sciences, Materials Sciences and Engineering Division, of the U.S. Department of Energy under Con-

tract No. DE-AC02-05CH11231. J.O., L.W., and A.L. received support for performing and analyzing optical measurements from the Gordon and Betty Moore Foundation's EPiQS Initiative through Grant GBMF4537 to J.O. at UC Berkeley. Sample growth was supported by the Gordon and Betty Moore Foundation's EPiQS Initiative Grant GBMF4374 to J.A. at UC Berkeley. T.M. is supported by the Gordon and Betty Moore Foundation's EPiQS Initiative Theory Center Grant to UC Berkeley. J.E.M. received support for travel from the Simons Foundation. The authors would like to thank Nobumichi Tamura for his help in performing crystal diffraction and orientation on beamline 12.3.2 at the Advanced Light Source. N. Tamura and the ALS are supported by the Director, Office of Science, Office of Basic Energy Sciences, of the U.S. Department of Energy under Contract No. DE-AC02-05CH11231.

Competing Interests: The authors declare that they have no competing financial interests.

Correspondence: Correspondence and requests for materials should be addressed to L.W. (email:liangwu@berkeley.edu) and J.O. (email:jworenstein@lbl.gov).

III. AUTHOR CONTRIBUTION

L.W. and J.O. conceived the project. L.W. and S.P. performed and contributed equally to the SHG measurements with assistance from E. T. and A. L.. L.W. and J.O. analyzed the data. T.M. and J.M. performed the model calculation. L.W., T.M. and J.O. performed the frequency scaling analysis. N.N. and J.A. grew the crystals and characterized the crystal structure. L.W., T.M. and J.O. wrote the manuscript. All authors commented on the manuscript.

IV. Supplementary Information for ‘‘Giant anisotropic nonlinear optical response in transition metal monpnictide Weyl semimetals’’

A. Dependence of SHG amplitude on polarization for different crystal and surfaces used in this study

In general, the polarization, \mathbf{P} , in materials has contributions from higher orders of the electric field, \mathbf{E} , in addition to the linear response, such that,

$$\mathbf{P} = \mathbf{P}_0 + \epsilon_0 \chi_e \mathbf{E} + \epsilon_0 \chi^{(2)} \mathbf{E}^2 + \dots \quad (1)$$

In noncentrosymmetric materials the second order term, $P_i^{(2)} = \chi_{ijk} E_j E_k$, that gives rise to frequency mixing, SHG, and optical rectification, is allowed[1, 2]. The latter two phenomena arise from excitation with a single frequency, such that there is an automatic symmetry with respect to permutation of the second and third indices. This motivates the use of a 3×6 second rank tensor d_{ij} instead of χ_{ijk} . The relation between d_{ij} and χ_{ijk} is as follows: the first index $i = 1, 2, 3$ in d_{ij} corresponds to $i = x, y, z$ in χ_{ijk} and the second index $j = 1 - 6$ in d_{ij} corresponds to $jk = xx, yy, zz, \frac{yz+zy}{2}, \frac{zx+xz}{2}, \frac{xy+yz}{2}$ in χ_{ijk} . In terms of the d tensor, the relation between second order polarization and electric field has the form,

$$\begin{bmatrix} P_1(2\omega) \\ P_2(2\omega) \\ P_3(2\omega) \end{bmatrix} = \begin{bmatrix} d_{11} & d_{12} & d_{13} & d_{14} & d_{15} & d_{16} \\ d_{21} & d_{22} & d_{23} & d_{24} & d_{25} & d_{26} \\ d_{31} & d_{32} & d_{33} & d_{34} & d_{35} & d_{36} \end{bmatrix} \begin{bmatrix} E_1^2(\omega) \\ E_2^2(\omega) \\ E_3^2(\omega) \\ 2E_2(\omega)E_3(\omega) \\ 2E_1(\omega)E_3(\omega) \\ 2E_1(\omega)E_2(\omega) \end{bmatrix}. \quad (2)$$

For a crystal with effective point group symmetry $4mm$, the nonzero elements are $d_{15} = d_{24}$, $d_{31} = d_{32}$ and d_{33} . Note that TaAs family belongs to the non-symmorphic $I4_1md$ space group which has screw rotation instead of C_4 rotation. However, screw and C_4 rotation symmetries lead to the same constraints on $\chi^{(2)}$ in optics and therefore SHG is described by the $4mm$ point group in TaAs. Predictions based on Eq. 2 for the angular dependence of the SHG intensity for four scans that involve linear polarized light normally incident on the TaAs or TaP or NbAs (112) surface are given below. Eqs. 3 and 4 refer to scans where two polarizers are synchronously rotated to simulate rotation of the sample. I_{para} and I_{perp} correspond to generator and analyzer polarization set parallel and perpendicular, respectively,

$$I_{para}(\theta_1) = \frac{1}{27} |(d_{33} + 4d_{15} + 2d_{31}) \cos^3 \theta_1 + 3(2d_{15} + d_{31}) \sin^2 \theta_1 \cos \theta_1|^2, \quad (3)$$

$$I_{perp}(\theta_1) = \frac{1}{27} |(d_{33} - 2d_{15} + 2d_{31}) \cos^2 \theta_1 \sin \theta_1 + 3d_{31} \sin^3 \theta_1|^2. \quad (4)$$

Eqs. 5 and 6 refer to scans where the analyzer is fixed at 0° (parallel to $[1,1,-1]$) and 90° (parallel to $[1,-1,0]$), respectively, and the direction of linear polarization of the generator is scanned,

$$I_{0^\circ}(\theta_1) = \frac{1}{27} |(d_{33} + 4d_{15} + 2d_{31}) \cos^2 \theta_1 - d_{31} \sin^2 \theta_1|^2, \quad (5)$$

$$I_{90^\circ}(\theta_1) = \frac{1}{3} |d_{15}|^2 \sin 2\theta_1. \quad (6)$$

The remaining scan that provides independent information constraining the elements of the d tensor is a measurement of SHG circular dichroism, which is the difference in SHG intensity between left and right circular polarization. To lowest order in d_{ij} ,

$$I_{\sigma^+}(\theta_2) - I_{\sigma^-}(\theta_2) = \frac{2}{9} \text{Im}\{d_{15}d_{33}^*\} \sin 2\theta_2. \quad (7)$$

The circular dichroism in SHG is proportional to $Im(d_{33}d_{15}^*)$ and therefore measures the component of d_{15} that is out-of-phase with d_{33} . From comparison of the circular dichroism and linear polarization measurements we find a relative phase of $30^\circ (\pm 10^\circ)$ between d_{15} and d_{33} at 300 K.

The benchmark materials, GaAs and ZnTe, have the same point group $\bar{4}3m$, and the only nonzero components of the d tensor are $d_{14} = d_{25} = d_{36}$. For light normally incident on the ZnTe (110) surface, the SHG angular dependencies are,

$$I_{para}(\theta_1) = 6|d_{14}|^2 \cos^4 \theta_1 \sin^2 \theta_1, \quad (8)$$

$$I_{perp}(\theta_1) = |d_{14}|^2 (4 \cos \theta_1 \sin^2 \theta_1 - 2 \cos^3 \theta_1). \quad (9)$$

and for GaAs (111),

$$I_{para}(\theta_1) = |d_{14}|^2 \left(\frac{2\sqrt{6}\cos^3 \theta_1}{3} - 2\sqrt{6} \cos \theta_1 \sin^2 \theta_1 \right). \quad (10)$$

$$I_{perp}(\theta_1) = |d_{14}|^2 \left(\frac{2\sqrt{6}\sin^3 \theta_1}{3} - 2\sqrt{6} \cos^2 \theta_1 \sin \theta_1 \right). \quad (11)$$

B. Obtaining nonlinear response coefficients from benchmark materials

From Eq. 3, the peak SHG intensity from TaAs (112) is proportional to $|d_{\text{eff}}|^2/27$, where $d_{\text{eff}} \equiv d_{33} + 4d_{15} + 2d_{31}$. Peak SHG intensities from ZnTe (110) and GaAs (111) are proportional to $4|d_{14}|^2/3$ and $4|d_{14}|^2/6$, respectively. When measured in reflection, in addition to the nonlinear response coefficients, the SHG intensity depends on the index of refraction at the fundamental and the second harmonic frequencies. To compare SHG intensities from different compounds we use a formula derived by Bloembergen and Pershan [3],

$$\chi_R^{(2)} \equiv -\frac{E_R(2\omega)}{\epsilon_0 E(\omega)^2} = \frac{\chi^{(2)}}{(\epsilon^{1/2}(2\omega) + \epsilon^{1/2}(\omega))(\epsilon^{1/2}(2\omega) + 1)} T(\omega)^2. \quad (12)$$

where ϵ is the relative dielectric constant, ‘R’ stands for reflection geometry and $T(\omega) = \frac{2}{n(\omega)+1}$ is the Fresnel coefficient of the fundamental light. Values for index of refraction were taken from the literature: ZnTe[4], GaAs[5] and complex index of TaAs was measured by the method that can be found in Ref. 6. The correction factor turns out to be small, less than 20%, because the indices of refraction for the three compounds are similar (within 30% difference) in magnitude at the relevant frequencies. Without taking account of this correction, we obtain $|d_{33}| \sim 3000 \pm 450$ pV/m for TaAs by referring to the value of ZnTe[7].

After establishing the relative size of the d coefficients by the procedure described above, we used measurements of the absolute amplitude of d_{14} in ZnTe *et al.*[7] to obtain absolute amplitudes for GaAs and TaAs. As reported in the main text, we obtain $|d_{33}| \sim 3600$ pV/m in TaAs. Using the same procedure of referencing to ZnTe, we obtain $|d_{14}| \sim 380$ pV/m for GaAs, which agrees with the literature value[8].

-
- [1] Boyd, R. W. Nonlinear optics. Academic press, (2003).
 - [2] Shen, Y.-R., Principles of nonlinear optics. Wiley-Interscience. (1984).
 - [3] Bloembergen, N. & Pershan, P. Light waves at the boundary of nonlinear media. *Physical Review*, **128**, 606, (1962).
 - [4] Li, H.H. Refractive index of ZnS, ZnSe, and ZnTe and its wavelength and temperature derivatives. *Journal of physical and chemical reference data*, **13**, 103, (1984).
 - [5] Forouhi, A. & Bloomer, I. Optical properties of crystalline semiconductors and dielectrics. *Phys. Rev. B.*, **38**, 1865, (1988).
 - [6] Xu, B. *et al.* I. Optical spectroscopy of the Weyl semimetal TaAs *Phys. Rev. B.*, **93**, 121110, (2016).
 - [7] Wagner, H. P., Kuhnelt, M., Langbein, W. & Hvam, W. Dispersion of the second-order nonlinear susceptibility in ZnTe, ZnSe, and ZnS. *Physical Review B*, **58**, 10494, (1998).
 - [8] Bergfeld, S. & Daum, W. Second-harmonic generation in GaAs: Experiment versus theoretical predictions of $\chi^{(2)xyz}$ *Physical Review Letters*, **90**, 036801, (2003).
-